



# CHORUS

This is the accepted manuscript made available via CHORUS. The article has been published as:

## Superextremal spinning black holes via accretion

Tanja Bode, Pablo Laguna, and Richard Matzner

Phys. Rev. D **84**, 064044 — Published 29 September 2011

DOI: [10.1103/PhysRevD.84.064044](https://doi.org/10.1103/PhysRevD.84.064044)

# Super-Extremal Spinning Black Holes via Accretion

Tanja Bode,<sup>1</sup> Pablo Laguna,<sup>1</sup> and Richard Matzner<sup>2</sup>

<sup>1</sup>*Center for Relativistic Astrophysics and School of Physics  
Georgia Institute of Technology, Atlanta, Georgia 30332, USA*

<sup>2</sup>*Center for Relativity and Department of Physics  
University of Texas at Austin, Austin, Texas 78712, USA*

A Kerr black hole with mass  $M$  and angular momentum  $J$  satisfies the extremality inequality  $|J| \leq M^2$ . In the presence of matter and/or gravitational radiation, this bound needs to be reformulated in terms of local measurements of the mass and the angular momentum directly associated with the black hole. The isolated and dynamical horizon framework provides such quasi-local characterization of black hole mass and angular momentum. With this framework, it is possible in axisymmetry to reformulate the extremality limit as  $|J| \leq 2 M_H^2$ , with  $M_H$  the irreducible mass of the black hole computed from its apparent horizon area and  $J$  obtained using a rotational Killing vector field on the apparent horizon. The  $|J| \leq 2 M_H^2$  condition is also equivalent to requiring a non-negative black hole surface gravity. We present numerical experiments of an accreting black hole that temporarily violates this extremality inequality. The initial configuration consists of a single, rotating black hole surrounded by a thick, shell cloud of negative energy density. For these numerical experiments, we introduce a new matter-without-matter evolution method.

PACS numbers:

## I. INTRODUCTION

Kerr spacetimes, representing a spinning black hole (BH) in isolation, have a bound on the maximum allowed angular momentum. If  $M$  is the mass of the BH and  $J$  its angular momentum, the bound or *extremality condition* reads  $|J| \leq M^2$ . An extremal Kerr BH saturates this condition (i.e.  $|J| = M^2$ ). Kerr spacetimes violating the extremality condition (i.e.  $|J| > M^2$ ) have naked singularities instead of BHs. A natural question to ask then is whether more general BH spacetimes (e.g. BHs in the presence of matter, Maxwell fields, gravitational radiation and/or other BHs) are also subject to extremality conditions, thus precluding the existence of *super-extremal* BHs.

The existence of extremality conditions in more general BH spacetimes has been investigated in a series of papers by Ansorg and collaborators. These studies considered axisymmetric and stationary BHs surrounded by matter [1, 2]. In some cases, Maxwell fields were also included [3]. Of direct relevance to our work is the study by Ansorg and Petroff [4] demonstrating the feasibility of configurations with super-extremal BHs. More recently, in an initial data study of binary BHs with nearly extremal spins [5], each BH was found to have an inner, super-extremal apparent horizon (AH), but the outermost (and true) AH was sub-extremal.

As pointed out by Booth and Fairhurst [6], at the core of any study of BH extremality conditions is characterizing what one means by mass and angular momentum associated with the BH, namely distinguishing the “local” properties of the BH from those of its environment. As shown also in [6], the natural tools for such a task are those provided by the isolated and dynamical horizon framework [7]. Using this framework, Booth and Fairhurst [6] reformulated extremality conditions in

terms of restrictions on isolated and dynamical horizons, and introduced a parameter that determines how close a horizon is to extremality.

The goal of our work is to investigate the formation of a *super-extremal* BH in a dynamical setup using the tools of numerical relativity. Specifically, we consider a sub-extremal BH surrounded with a spherically symmetric cloud of negative energy density. As the BH accretes the cloud, its mass decreases and its angular momentum increases. As a consequence, the dimensionless spin parameter of the BH increases. This approach to spinning up a BH by decreasing its mass is complementary to the more astrophysically relevant case in which a BH spins up by gaining angular momentum from the material it swallows [8]. For clouds with enough negative energy density, we are able to build super-extremal BHs. The super-extremal state is, however, not stable. Non-axisymmetric instabilities develop, triggering emission of gravitational radiation that carried angular momentum.

Our study also introduces a new evolution scheme called matter-without-matter (MWM). The MWM approach consists of evolving the spacetime geometry using the BSSN [9] evolution equations without their matter source terms, namely the vacuum version of the evolution equations. The matter fields are constructed at each step from the BSSN constraints (Hamiltonian, momentum and connection constraints). In addition, the stress energy tensor is required to have a form for which the matter source terms in the BSSN evolution equations vanish. The approach is reminiscent of the constraint-violating BH initial data evolved in a previous study [10]. Our MWM method differs, however, from work with hydro-without-hydro evolutions [11, 12]. In those studies, the matter hydrodynamics was pre-prescribed and was used as input to construct the source terms in the evolution equations.

The paper is organized as follows: In Section II, we summarize the extremality conditions and discuss the condition used in our numerical experiments to identify the emergence of super-extremality. Section III describes the MWM evolution approach and the conditions that the matter content must satisfy. In Sec. IV, we describe the initial data configurations used in our simulations. Results showing the formation of a super-extremal BH are given in Sec. V. In Sec. VI, we address the degree to which the null energy condition is satisfied by our spacetimes. In Sec. VII, we investigate the late-time behavior in terms of the constraints. Conclusions are presented in Sec. VIII. The numerical simulations and results were obtained with the Maya Code as described in Refs. [10, 13, 14]. Subscripts  $a, b, c, \dots$  will denote space-time indices while  $i, j, k, \dots$  will denote spatial indices. We use units in which  $G = c = 1$ .

## II. EXTREMALITY CONDITIONS

There are three notions of extremality in stationary, asymptotically flat BH spacetimes (see [6] for details): i) the angular momentum  $J$  and mass  $M$  of a BH satisfy the bound  $\chi \equiv |J|/M^2 \leq 1$ ; ii) the surface gravity  $\kappa$  of a BH satisfies the bound  $\kappa \geq 0$ ; and iii) the interior of a non-extremal BH contains trapped surfaces, while there are no trapped surfaces in the interior of an extremal BH.

The first notion of extremality ( $\chi \leq 1$ ) compares the Christodoulou mass [15]  $M$  to the angular momentum  $J$  of the BH. The Christodoulou mass is given by

$$M^2 \equiv M_H^2 + \frac{J^2}{4M_H^2} = M_H^2 \left[ 1 + \left( \frac{J}{2M_H^2} \right)^2 \right]. \quad (1)$$

$M_H$  is a local measure of the BH mass, called the irreducible mass. The mass is computed from  $M_H = \sqrt{A/16\pi}$ , with  $A$  the area of the AH of the BH. The angular momentum  $J$  is also obtained locally using rotational Killing vectors on the AH [7].

The surface gravity  $\kappa$  of stationary and axisymmetric BHs is obtained from  $k^b \nabla_b k^a = \kappa k^a$ , where  $k^a$  describes the Killing vector that becomes null at the horizon. For Kerr space-times, the surface gravity takes the form

$$\kappa = \frac{1}{2M_H} \frac{(1 - \chi^2)^{1/2}}{[1 + (1 - \chi^2)^{1/2}]}. \quad (2)$$

Evident from Eq. (2) is the equivalence between the first two notions of extremality, namely  $\chi \leq 1$  and  $\kappa \geq 0$ .

The goal of our study is to investigate conditions under which the extremality conditions  $\chi \leq 1$  and  $\kappa \geq 0$  are violated. Using  $\chi$  for this purpose has, however, the following drawback. From Eq. (1), it is not difficult to show that

$$\left( \frac{2M_H^2}{M^2} - 1 \right)^2 = 1 - \frac{J^2}{M^4} = 1 - \chi^2. \quad (3)$$

Thus, by construction  $\chi \leq 1$ . It has been then suggested [5, 6] that a quantity more suitable to investigate extremality is  $\zeta \equiv |J|/(2M_H^2)$ , or equivalently  $\zeta \equiv 8\pi|J|/A$  [16]. In terms of  $\zeta$ , the spin parameter  $\chi$  and the surface gravity  $\kappa$  take the form

$$\chi = 1 - \frac{(1 - \zeta)^2}{1 + \zeta^2} \quad (4)$$

$$\kappa = \frac{1 - \zeta^2}{4M}, \quad (5)$$

respectively. Thus, for  $\zeta \leq 1$ , one recovers the extremality conditions  $\chi \leq 1$  and  $\kappa \geq 0$ . The advantage of the new spin parameter  $\zeta$  is that values  $\zeta > 1$  are allowable. Furthermore, for  $\zeta > 1$ , one still has  $\chi \leq 1$ , but the surface gravity, on the other hand, becomes negative.

In Ref. [6], a new notion of extremality was introduced in terms of  $\zeta$ : A BH is said to be *sub-extremal* if  $\zeta < 1$  ( $\kappa > 0$ ), *extremal* if  $\zeta = 1$  ( $\kappa = 0$ ), and *super-extremal* if  $\zeta > 1$  ( $\kappa < 0$ ). This new notion of extremality is derived assuming that: i) the spacetime is axisymmetric; ii) the null energy condition is satisfied; and iii) the cross sections of the horizon are embeddable in Euclidean  $\mathbb{R}^3$ . A generalization of extremality, relaxing the axisymmetry and embeddability assumptions but keeping the null energy condition, is also possible [6].

## III. MATTER-WITHOUT-MATTER EVOLUTIONS

Our study introduces also an evolution scheme that we call the *matter-without-matter* method. Under the MWM approach, the geometry of the spacetime is evolved using the vacuum or source-free BSSN evolution equations. There is no need for matter evolution equations. As we shall show next, the matter fields are obtained at every step of the evolution from the BSSN constraints (Hamiltonian, momentum and connection constraints) together with *equations-of-state*. To demonstrate how the MWM works, we will re-derive the BSSN evolution equations, taking explicitly into account a matter content that is *invisible* to these equations.

The BSSN formulation of the Einstein equations consists of a set of evolution equations for the conformal metric  $\tilde{\gamma}_{ij}$ , the conformal factor  $\phi$ , the trace of the physical extrinsic curvature  $K$ , the trace-free part of the conformal extrinsic curvature  $\tilde{A}_{ij}$ , and the connection  $\tilde{\Gamma}^i \equiv \tilde{\gamma}^{jk} \tilde{\Gamma}_{jk}^i = -\partial_j \tilde{\gamma}^{ij}$  (see Ref. [17] for details). The evolution equations for  $\phi$ ,  $\tilde{\gamma}_{ij}$  and  $K$  are respectively:

$$\partial_o \phi = -\frac{1}{6} \alpha K \quad (6)$$

$$\partial_o \tilde{\gamma}_{ij} = -2\alpha \tilde{A}_{ij} \quad (7)$$

$$\begin{aligned} \partial_o K &= -\nabla_i \nabla^i \alpha + \alpha \left( \tilde{A}^{ij} \tilde{A}_{ij} + \frac{1}{3} K^2 \right) \\ &\quad + 4\pi \alpha (\rho + S), \end{aligned} \quad (8)$$

$\nabla$  denotes covariant differentiation with respect to the physical metric  $\gamma_{ij} = e^{4\phi}\tilde{\gamma}_{ij}$ ,  $\alpha$  is the lapse function, and  $\beta^i$  is the shift vector; we define  $\partial_o \equiv \partial_t - \mathcal{L}_\beta$ , with  $\mathcal{L}_\beta$  the spatial Lie derivative along  $\beta^i$ . Above, the source terms  $\rho$  and  $S = \gamma^{ij}S_{ij}$  are obtained from

$$\rho = n^a n^b T_{ab} \quad (9)$$

$$j^i = -\gamma^{ia} n^b T_{ab} \quad (10)$$

$$S_{ij} = \gamma_i^a \gamma_j^b T_{ab} \quad (11)$$

with  $T_{ab}$  the stress-energy tensor and with  $n^a$  the unit, time-like normal to the constant  $t$  hypersurfaces. That is, the stress-energy tensor has the following form:

$$T_{ab} = \rho n_a n_b + 2j_{(a} n_{b)} + S_{ab}. \quad (12)$$

Before considering the evolution equations for  $\tilde{A}_{ij}$  and  $\tilde{\Gamma}^i$ , we need to recall the constraints in the BSSN formulation. As with any 3+1 formulation of the Einstein field equations of general relativity, the BSSN formulation involves the Hamiltonian and momentum constraints. In terms of the BSSN variables, these constraints read:

$$e^{-5\phi}\tilde{\nabla}_i\tilde{\nabla}^i e^\phi - \frac{e^{-4\phi}}{8}\tilde{R} + \frac{1}{8}\tilde{A}^{ij}\tilde{A}_{ij} - \frac{1}{12}K^2 = -2\pi\rho \quad (13)$$

and

$$e^{-6\phi}\tilde{\nabla}_j(e^{6\phi}\tilde{A}^{ij}) - \frac{2}{3}\tilde{\nabla}^i K = 8\pi j^i, \quad (14)$$

respectively. In addition, the BSSN formulation introduces the following new constraints:

$$\mathcal{A} = \tilde{A}^i{}_i = 0 \quad (15)$$

$$\mathcal{S} = \tilde{\gamma} - 1 = 0 \quad (16)$$

$$\mathcal{G}^i = \tilde{\Gamma}^i + \partial_j \tilde{\gamma}^{ij} = 0. \quad (17)$$

Our Maya Code actively imposes the trace-free (15) and unit-determinant (16) constraints. On the other hand, in numerical evolutions, the Hamiltonian (13), momentum (14) and connection (17) constraints are not explicitly imposed. One of the main virtues of the BSSN formulation is precisely that aspect. Namely, in the course of a BSSN evolution, the constraints (13), (14) and (17) are preserved within tolerable levels. In our MWM scheme, the Hamiltonian, momentum and connection constraints play a different role. The Hamiltonian and momentum constraints are used to construct  $\rho$  and  $j^i$ , respectively. But more importantly, in MWM simulations (see below),  $\mathcal{G}^i$  evolves away from  $\mathcal{G}^i = 0$  and provides a key ingredient in determining the dynamics of the matter content. For this reason, we need next to re-derive the evolution equations for  $\tilde{A}_{ij}$  and  $\tilde{\Gamma}^i$  without imposing the  $\mathcal{G}^i = 0$  constraint.

For the  $\tilde{A}_{ij}$  evolution equation, the only place where  $\mathcal{G}^i$  enters is in the Ricci tensor  $R_{ij}$ , which is normally

computed from  $R_{ij} = \tilde{R}_{ij} + R_{ij}^\phi$  with

$$\begin{aligned} \tilde{R}_{ij} &= -\frac{1}{2}\tilde{\gamma}^{lm}\partial_l\partial_m\tilde{\gamma}_{ij} \\ &+ \tilde{\gamma}^{lm}\left(2\tilde{\Gamma}_{l(i}\tilde{\Gamma}_{j)km} + \tilde{\Gamma}_{im}^k\tilde{\Gamma}_{klj}\right) \\ &+ \tilde{\gamma}_{k(i}\partial_{j)}\tilde{\Gamma}^k + \tilde{\Gamma}^k\tilde{\Gamma}_{(ij)k}, \end{aligned} \quad (18)$$

and

$$\begin{aligned} R_{ij}^\phi &= -2\left(\tilde{\nabla}_i\tilde{\nabla}_j\phi + \tilde{\gamma}_{ij}\tilde{\nabla}_k\tilde{\nabla}^k\phi\right) \\ &+ 4\left(\tilde{\nabla}_i\phi\tilde{\nabla}_j\phi - \tilde{\gamma}_{ij}\tilde{\nabla}_k\phi\tilde{\nabla}^k\phi\right), \end{aligned} \quad (19)$$

respectively. If  $\mathcal{G}^i \neq 0$ , the Ricci tensor  $\tilde{R}_{ij}$  acquires an additional term, namely

$$\begin{aligned} \tilde{R}_{ij} &\rightarrow \tilde{R}_{ij} - \frac{1}{2}\tilde{\gamma}^{lm}\partial_l\partial_m\tilde{\gamma}_{ij} \\ &+ \tilde{\gamma}^{lm}\left(2\tilde{\Gamma}_{l(i}\tilde{\Gamma}_{j)km} + \tilde{\Gamma}_{im}^k\tilde{\Gamma}_{klj}\right) \\ &+ \tilde{\gamma}_{k(i}\partial_{j)}\tilde{\Gamma}^k + \tilde{\Gamma}^k\tilde{\Gamma}_{(ij)k} \\ &- \tilde{\gamma}_{k(i}\partial_{j)}\mathcal{G}^k - \mathcal{G}^k\tilde{\Gamma}_{(ij)k}. \end{aligned} \quad (20)$$

Therefore,  $R_{ij}$  is given instead as  $R_{ij} = \tilde{R}_{ij} + R_{ij}^\phi + 8\pi M_{ij}$  with  $\tilde{R}_{ij}$  and  $R_{ij}^\phi$  given by (18) and (19), respectively, and

$$M_{ij} \equiv -\frac{1}{8\pi}\left(\tilde{\gamma}_{k(i}\partial_{j)}\mathcal{G}^k + \mathcal{G}^k\tilde{\Gamma}_{(ij)k}\right). \quad (21)$$

With  $M_{ij}$  viewed as an additional source term, one can follow the standard BSSN derivation [17] of the evolution equation for  $\tilde{A}_{ij}$  and arrive at:

$$\begin{aligned} \partial_o\tilde{A}_{ij} &= e^{-4\phi}\left[-\tilde{\nabla}_i\tilde{\nabla}_j\alpha + \alpha R_{ij} - 8\pi\alpha(S_{ij} - M_{ij})\right]^{TF} \\ &+ \alpha(K\tilde{A}_{ij} - 2\tilde{A}_{ik}\tilde{A}^k{}_j), \end{aligned} \quad (22)$$

where  $TF$  denotes the trace-free part of the tensor.

The remaining equation to consider is the evolution equation for  $\tilde{\Gamma}^i$ . Once again, we will derive this equation without the assumption that the constraint  $\mathcal{G}^i = 0$  holds. The starting point is the time derivative of  $\tilde{\Gamma}^i = -\partial_j\tilde{\gamma}^{ij} + \mathcal{G}^i$ :

$$\partial_t\tilde{\Gamma}^i = -\partial_j\partial_t\tilde{\gamma}^{ij} + \partial_t\mathcal{G}^i. \quad (23)$$

On the other hand, from Eq. (7):

$$\begin{aligned} \partial_t\tilde{\gamma}^{ij} &= 2\alpha\tilde{A}^{ij} + \beta^k\partial_k\tilde{\gamma}^{ij} \\ &- \tilde{\gamma}^{ik}\partial_k\beta^j - \tilde{\gamma}^{jk}\partial_k\beta^i + \frac{2}{3}\tilde{\gamma}^{ij}\partial_k\beta^k, \end{aligned} \quad (24)$$

which after differentiation reads

$$\begin{aligned} \partial_t\partial_j\tilde{\gamma}^{ij} &= \partial_j(2\alpha\tilde{A}^{ij}) \\ &+ \beta^k\partial_k\partial_j\tilde{\gamma}^{ij} - \partial_j\tilde{\gamma}^{jk}\partial_k\beta^i + \frac{2}{3}\partial_j\tilde{\gamma}^{ij}\partial_k\beta^k \\ &- \tilde{\gamma}^{jk}\partial_j\partial_k\beta^i - \frac{1}{3}\tilde{\gamma}^{ij}\partial_j\partial_k\beta^k. \end{aligned} \quad (25)$$

Thus, Eq. (23) becomes

$$\begin{aligned} \partial_t \tilde{\Gamma}^i &= -2 \tilde{A}^{ij} \partial_j \alpha - 2 \alpha \partial_j \tilde{A}^{ij} \\ &- \beta^k \partial_k \partial_j \tilde{\gamma}^{ij} + \partial_j \tilde{\gamma}^{jk} \partial_k \beta^i - \frac{2}{3} \partial_j \tilde{\gamma}^{ij} \partial_k \beta^k \\ &+ \tilde{\gamma}^{jk} \partial_j \partial_k \beta^i + \frac{1}{3} \tilde{\gamma}^{ij} \partial_j \partial_k \beta^k + \partial_t \mathcal{G}^i. \end{aligned} \quad (26)$$

Next we use the momentum constraint (14) to eliminate the term involving  $\partial_j \tilde{A}^{ij}$ , and rewrite (26) as:

$$\begin{aligned} \partial_t \tilde{\Gamma}^i &= -2 \tilde{A}^{ij} \partial_j \alpha - 16 \pi \alpha \tilde{\gamma}^{ij} j_j \\ &- 2 \alpha \left( -\tilde{\Gamma}_{jk}^i \tilde{A}^{jk} - 6 \tilde{A}^{ij} \partial_j \phi + \frac{2}{3} \tilde{\gamma}^{ij} \partial_j K \right) \\ &- \beta^k \partial_k \partial_j \tilde{\gamma}^{ij} + \partial_j \tilde{\gamma}^{jk} \partial_k \beta^i - \frac{2}{3} \partial_j \tilde{\gamma}^{ij} \partial_k \beta^k \\ &+ \tilde{\gamma}^{jk} \partial_j \partial_k \beta^i + \frac{1}{3} \tilde{\gamma}^{ij} \partial_j \partial_k \beta^k + \partial_t \mathcal{G}^i. \end{aligned} \quad (27)$$

With the help of  $\partial_j \tilde{\gamma}^{ij} = -\tilde{\Gamma}^i + \mathcal{G}^i$ , we obtain

$$\begin{aligned} \partial_t \tilde{\Gamma}^i &= -2 \tilde{A}^{ij} \partial_j \alpha - 16 \pi \alpha \tilde{\gamma}^{ij} j_j \\ &- 2 \alpha \left( -\tilde{\Gamma}_{jk}^i \tilde{A}^{jk} - 6 \tilde{A}^{ij} \partial_j \phi + \frac{2}{3} \tilde{\gamma}^{ij} \partial_j K \right) \\ &+ \beta^j \partial_j \tilde{\Gamma}^i - \tilde{\Gamma}^j \partial_j \beta^i + \frac{2}{3} \tilde{\Gamma}^i \partial_j \beta^j \\ &- \beta^j \partial_j \mathcal{G}^i + \mathcal{G}^j \partial_j \beta^i - \frac{2}{3} \mathcal{G}^i \partial_j \beta^j \\ &+ \tilde{\gamma}^{jk} \partial_j \partial_k \beta^i + \frac{1}{3} \tilde{\gamma}^{ij} \partial_j \partial_k \beta^k + \partial_t \mathcal{G}^i, \end{aligned} \quad (28)$$

which can be rewritten as

$$\begin{aligned} \partial_o \tilde{\Gamma}^i &= -2 \tilde{A}^{ij} \partial_j \alpha \\ &- 2 \alpha \left( -\tilde{\Gamma}_{jk}^i \tilde{A}^{jk} - 6 \tilde{A}^{ij} \partial_j \phi + \frac{2}{3} \tilde{\gamma}^{ij} \partial_j K \right) \\ &+ \tilde{\gamma}^{jk} \partial_j \partial_k \beta^i + \frac{1}{3} \tilde{\gamma}^{ij} \partial_j \partial_k \beta^k \\ &+ \partial_o \mathcal{G}^i - 16 \pi \alpha \tilde{\gamma}^{ij} j_j, \end{aligned} \quad (29)$$

with both  $\tilde{\Gamma}^i$  and  $\mathcal{G}^i$  treated as vector densities of weight 2/3. Equations (6), (7), (8), (13), (14), (22) and (29) constitute the basis of our MWM method.

From the form of the stress-energy tensor (12), we see that without any further assumptions, our set of equations is not able to determine  $S_{ij}$ . The essence of a MWM evolution is then to impose that matter evolves in such a way that the source terms in (8), (22) and (29) vanish, namely

$$\rho + S = 0 \quad (30)$$

$$(S_{ij} - M_{ij})^{TF} = 0 \quad (31)$$

$$\partial_o \mathcal{G}^i - 16 \pi \alpha e^{-4 \phi} j^i = 0. \quad (32)$$

These conditions imply that the stress-energy tensor (12) takes the following form:

$$T_{ab} = \rho \left( n_a n_b - \frac{1}{3} \gamma_{ab} \right) + 2 j_{(a} n_{b)} + \gamma_a^i \gamma_b^j M_{ij}^{TF}. \quad (33)$$

The obvious advantage of the MWM method is the direct use of a vacuum (e.g. black hole) BSSN evolution code to construct the spacetime geometry. The matter fields  $\rho$ ,  $j^i$  and  $\mathcal{G}^i$  are obtained after every step from the Hamiltonian (13), momentum (14) and connection (17) constraints. Since the MWM method can be also viewed as evolving constraint violating data, there are no guarantees that the method is capable of producing stable evolutions. A general proof of the conditions that the initial data have to satisfy in order for the MWM to yield stable evolutions is beyond the scope of this study. We have found, however, that the set of configurations and evolutions for the present study on super-extremality were all numerically stable.

#### IV. INITIAL SETUP

Our study consists of a single, spinning BH puncture [18] enclosed by a thick, spherically symmetric, shell cloud of (in most cases negative) energy density. The shell surrounding the BH has a Gaussian profile and is initially static, with stress-energy tensor given by  $T_{ab} = \rho (n_a n_b - \gamma_{ab}/3)$ . Specifically, with this choice of stress-energy tensor, initially  $j^i = \mathcal{G}^i = \partial_o \mathcal{G}^i = 0$ .

Vanishing  $j^i$  implies that the momentum constraint reduces to the vacuum case. One can thus directly use the Bowen and York extrinsic curvature solutions for a spinning puncture [19]:

$$\hat{A}_{ij} = -\frac{3}{r^3} (\epsilon_{ilk} \hat{r}_j + \epsilon_{jlk} \hat{r}_i) \hat{r}^i J^k, \quad (34)$$

with  $\hat{r}^i$  the radial unit vector and  $J^i$  the puncture's angular momentum. Constructing initial data requires then solving only the Hamiltonian constraint [20]

$$\Delta \psi + \frac{1}{8} \psi^{-7} \tilde{A}_{ij} \tilde{A}^{ij} + 2 \pi \psi^5 \rho = 0 \quad (35)$$

with  $\hat{A}_{ij}$  given by (34) and  $\Delta$  the flat Laplacian. Notice that the standard assumptions of conformal flatness and vanishing trace of the extrinsic curvature have been used. Once a solution to Eq. (35) is found, the initial data for the spatial metric and the extrinsic curvature are obtained from  $\gamma_{ij} = \psi^4 \eta_{ij}$  and  $K_{ij} = \psi^{-2} \hat{A}_{ij}$ , respectively.

To solve Eq. (35), we use the puncture ansatz  $\psi = 1 + m_p/(2r) + u$ , with  $m_p$  the puncture's bare mass parameter. We choose the source  $\rho$  as:

$$\rho = \rho_o e^{-(r-r_o)^2/\sigma^2} \left( 1 + \frac{m_p}{2r} \right)^{-5}, \quad (36)$$

and the bare angular momentum as  $J^i = J \hat{z}^i$ . For all our simulations, we set  $J = 0.8$ . The last factor in (36) is needed for regularity at the location of the puncture.



Thus, Eq. (35) becomes:

$$\Delta u + \frac{18}{8} \frac{J^2 r \sin^2 \theta}{(r + m_p/2 + u r)^7} + 2\pi \left( \frac{r + m_p/2 + u r}{r + m_p/2} \right)^5 \rho_o e^{-(r-r_o)^2/\sigma^2} = 0, \quad (37)$$

with  $\hat{r}^i \hat{z}^j \eta_{ij} = \cos \theta$ .

The parameters  $r_o$  and  $\sigma$  are chosen to favor the accretion of most of the shell by the BH in evolution time-scales of  $\lesssim 40 M$ . The energy density amplitude parameter  $\rho_o$  is the *knob* that controls the mass associated with the shell, and thus regulates the total ADM mass  $M_o$  in the initial data.

Our approach to breaking the extremality bound  $\zeta \equiv |J|/(2M_H^2)$  is to not only increase the angular momentum  $J$  of the BH, but most importantly to decrease its mass  $M_H$ . To accomplish this, we endow the shell surrounding the BH with a negative mass, which decreases the BH's mass as it gets accreted.

It should be noted that in isolation any spinning puncture that models a rotating BH has a small ( $\lesssim 0.1\%$  of the total energy) spurious amount of gravitational radiation. This spurious radiation carries away a burst of angular momentum [21]; this amount, however, is small and does not affect the conclusions from our numerical experiment.

| Run | $r_o/M_o$ | $\sigma/M_o$ | $\rho_o M_o^2$         | $m_p/M_o$ | $\chi_o$ |
|-----|-----------|--------------|------------------------|-----------|----------|
| V0  | –         | –            | 0                      | 0.62      | 0.80     |
| V1  | 0.88      | 0.88         | $+7.03 \times 10^{-3}$ | 0.55      | 0.62     |
| V2  | 1.03      | 1.03         | $-3.77 \times 10^{-4}$ | 0.64      | 0.85     |
| V3  | 1.07      | 1.07         | $-1.05 \times 10^{-3}$ | 0.71      | 0.90     |
| V4  | 1.18      | 1.18         | $-1.72 \times 10^{-3}$ | 0.72      | 1.12     |
| V5  | 1.23      | 1.23         | $-2.00 \times 10^{-3}$ | 0.76      | 1.20     |

TABLE I: Initial parameters defining the matter shell ( $r_o, \sigma, \rho_o$ ). The last two columns display the puncture mass parameter  $m_p$  and ADM spin parameter  $\chi_o = J_o/M_o^2$ . All parameters are given in units of the ADM mass  $M_o$ .

Table I shows the parameters used for our simulations: the shell parameters ( $r_o, \sigma, \rho_o$ ) and the puncture mass  $m_p$ . These quantities and further results are given in dimensionless units in terms of the ADM mass  $M_o$ . The last column in Table I reports for each simulation the total spin parameter  $\chi_o \equiv J_o/M_o^2$ , with  $J_o$  the total ADM angular momentum. Since  $\chi_o$  is associated with the ADM mass and angular momentum of the space-time, it is not subject to an extremality condition. In particular,  $\chi_o$  includes angular momentum from outside the horizon. Notice that case V0 consists of a single puncture in vacuum. This case is used as a control run.

Case V1 is a fiducial evolution with a *positive* energy density shell. Cases V2–V5 contain shells with increasingly negative energy density. They are the central piece of our study. Table II gives the initial values for the irreducible  $M_H$  and Christodoulou  $M$  masses for each case. The table also shows the initial values of the BH's spin parameters  $\chi = J/M^2$ ,  $\zeta = |J|/(2M_H^2)$ , and its surface gravity  $\kappa$ .

| Run | $M_H/M_o$ | $M/M_o$ | $\chi$ | $\zeta$ | $\kappa M_o$ |
|-----|-----------|---------|--------|---------|--------------|
| V0  | 0.886     | 0.994   | 0.810  | 0.511   | 0.209        |
| V1  | 0.794     | 0.886   | 0.796  | 0.496   | 0.237        |
| V2  | 0.908     | 1.021   | 0.814  | 0.515   | 0.202        |
| V3  | 0.958     | 1.071   | 0.800  | 0.499   | 0.196        |
| V4  | 1.020     | 1.156   | 0.830  | 0.533   | 0.175        |
| V5  | 1.056     | 1.120   | 0.835  | 0.538   | 0.168        |

TABLE II: Initial irreducible mass  $M_H$ , Christodoulou mass  $M$ , dimensionless spin parameters  $\chi = J/M^2$  and  $\zeta = |J|/(2M_H^2) = 8\pi|J|/A$ , and surface gravity  $\kappa$  of the BH in units of the total ADM mass  $M_o$ .

Although we are dealing with a single BH, the numerical simulations are challenging. As the BH approaches extremality, the horizon undergoes extreme pancake-like deformation. Because of this severe deformation, in order to capture the dynamics in the vicinity of the BH and to have a chance of locating its AH, we were forced to use meshes with  $104^2 \times 52$  grid point shapes, and resolutions in the finest mesh of at least  $M/200$ , in addition to using 6th-order accurate finite differencing. For some of the cases, we carried out simulations with resolutions of  $M/167$  in the finest mesh to investigate the dependence of our results with resolution. We did not find noticeable differences regarding the onset of super-extremality. Resolution effects were mostly visible in tracking the AH.

## V. SUPER-EXTREMAL BLACK HOLES

We evolved the series of runs described in Table I. As previously stated, the case V0 is a control simulation to show that in the absence of matter, the BH mass and angular momentum indeed remain constant. For all the non-vacuum cases, the shell is absorbed early in the evolution. As a consequence, the mass  $M_H$  of the BH changes, increasing for the positive energy case V1 and decreasing for the remaining negative energy cases V2–V5.

The case V1 involving a positive energy density shell demonstrates an important feature of our data: the shell of matter has negative angular momentum and positive mass (see Figure 1). The BH mass increases and the spin decreases as the shell is absorbed. (The time axis

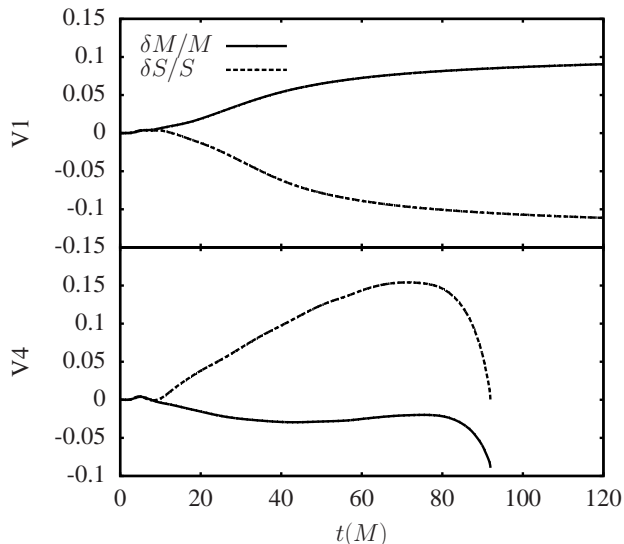


FIG. 1: Fractional change of the Christodoulou mass (solid) and spin (dotted) for the cases of V1 (top) and V4 (bottom).

in all figures is given in units of the initial Christodoulou mass of the BH.) Figure 1 also shows the behavior of the BH mass and angular momentum for the V4 case with a negative energy shell. The Equivalence Principle indicates that motion of test bodies is independent of their mass (even the sign of their mass) [22]. While our shells are not test bodies, we do expect the motion of the shells for the V1 positive mass case and the V4 negative mass case to be similar. We thus anticipate and find, for example in V4, that as the negative mass shell falls into the BH, the BH mass *decreases* and the BH angular momentum *increases* (see Figure 1), thus indicating that our negative energy shells have initially *positive* angular momentum.

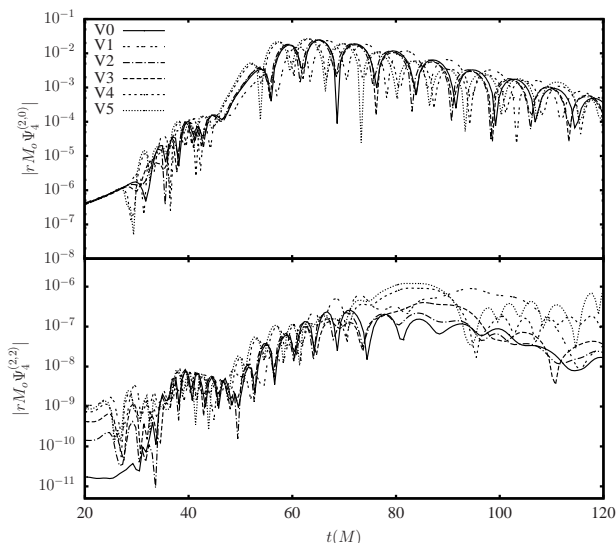


FIG. 2: Modes (2,0) and (2,2) of the Weyl scalar  $\Psi_4$  for all cases in the first 120  $M$  of evolution time.

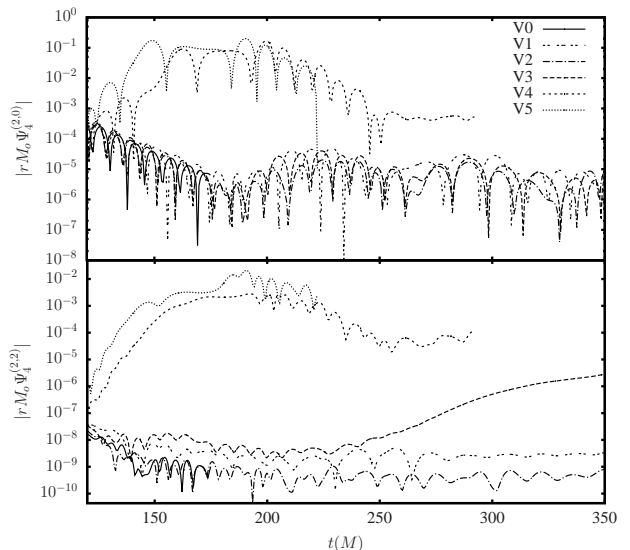


FIG. 3: Modes (2,0) and (2,2) of the Weyl scalar  $\Psi_4$  for all cases after 150  $M$  of evolution time.

As noted before, for all cases regardless of the energy density sign, we have chosen a matter configuration that is axisymmetric. However, as the matter spirals in and is swallowed by the BH, axisymmetry is not preserved. In the next section we will show evidence of non-axisymmetric accretion. This accretion, however, is ineffective at triggering deformations in the BH horizon. The BH horizon remains for practical purposes axisymmetric, and thus we are able to define a rotational Killing vector to compute the spin. Nevertheless, the deformations on the BH are large enough to allow for gravitational wave emission. The first emission occurs early on around  $t \sim 40 M$ . This is due to the spurious gravitational radiation in spinning punctures mentioned in the previous section. Details of this emission can be seen in Figure 2 where we show the (2,0) and (2,2) modes of the Weyl scalar  $\Psi_4$ . Around  $t \sim 60 M$ , the non-axisymmetric deformations from the accretion trigger a larger burst of gravitational radiation followed by quasi-normal ringing (see top panel Fig. 2). Notice from the bottom panel of Fig. 2 that the (2,2) mode, which could potentially carry angular momentum, is slightly stronger for the V4 and V5 cases. At late times,  $t > 150 M$ , non-axisymmetric instabilities trigger a much stronger additional burst of radiation for those two cases, as seen in Figure 3. As a consequence, the BH loses angular momentum.

Figure 4 shows the core of our study, namely the evolution of the spin parameter  $\zeta$  during the spacetime evolution. As expected,  $\zeta$  is constant in the V0 case. Also expected in case V1, with a positive energy density shell, is the decrease of the spin parameter  $\zeta$  of the BH due to the monotonic increase (decrease) of its mass (spin) observed in Fig. 1.

Cases V2–V5, with their negative energy density shells, are our main focus. As the shell is swallowed, the mass of the BH decreases monotonically since it accretes negative

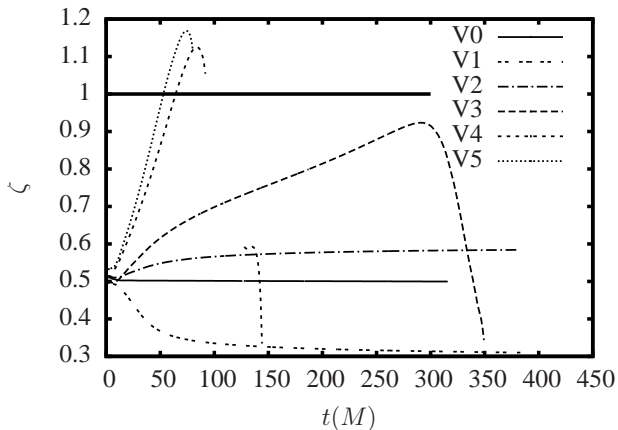


FIG. 4: Spin parameter  $\zeta$  as a function of evolution time.

mass. Furthermore, given that our negative energy shells have positive angular momentum, the spin of the BH will monotonically increase during the accretion. When taken together, the increase in spin and decrease in mass yield the observed growth of  $\zeta$  in Fig. 4. Notice from Fig. 4 that the larger the negative energy density of the shell, the faster the increase experienced by  $\zeta$ . Also, only the cases V4 and V5 breach the extremality bound  $\zeta = 1$ . These cases are the ones in which  $\chi_o > 1$  initially (see Table I). V4 becomes super-extremal at a time  $\sim 65 M$  and V5 at  $\sim 45 M$ . In both cases,  $\zeta$  continues to grow until it reaches a maximum, at  $\sim 85 M$  for V4 and  $\sim 70 M$  for V5. The drop in  $\zeta$  after reaching the maximum in V4 and V5 is due to the emission of angular momentum. The BH is not able to sustain super-extremality and simultaneously retain axisymmetry.

Fig. 4 also shows that after V4 and V5 reach a maximum, the  $\zeta$  lines terminate. This signals the time when we are no longer able to locate the AH of the BH. We have investigated whether the loss of the horizon is real or due to numerical effects. Simulations at different resolutions tells us that most likely the loss of the horizon is a numerical artifact: the last horizon times depend on resolution. The horizon undergoes a severe pancake deformation that the AH tracker is not able to handle because of the lack of resolution. We stress that the simulation does not crash; we only lose the horizon. This should not be viewed as “strange” since it is well known that stable puncture simulations do not resolve the puncture nor its immediate vicinity. If the horizon is too small, as with rapidly spinning BHs, the horizon is in danger of entering the under-resolved region near the puncture.

Notice in Fig. 4 that for V4 around  $150 M$ , when  $\zeta$  becomes again subcritical, we are again able to find the AH, albeit only briefly. Although the value of  $\zeta$  has significantly decreased, the shape of the horizon remains pancake-like, thus the challenge of locating the horizon remains. Since the AH shape is coordinate dependent, we are currently investigating modifications to the puncture gauges that alleviate the horizon deformations, giving us

a better chance of locating the horizon.

Finally, it is evident in Fig. 4 that  $\zeta$  increases in the sub-extremal cases V2 and V3. V2 gives hints of reaching an asymptotic value at later times. On the other hand, V3 has an approximate linear growth between  $75 M$  and  $300 M$  when it saturates at  $\zeta \sim 0.92$ .

## VI. NULL ENERGY CONDITION

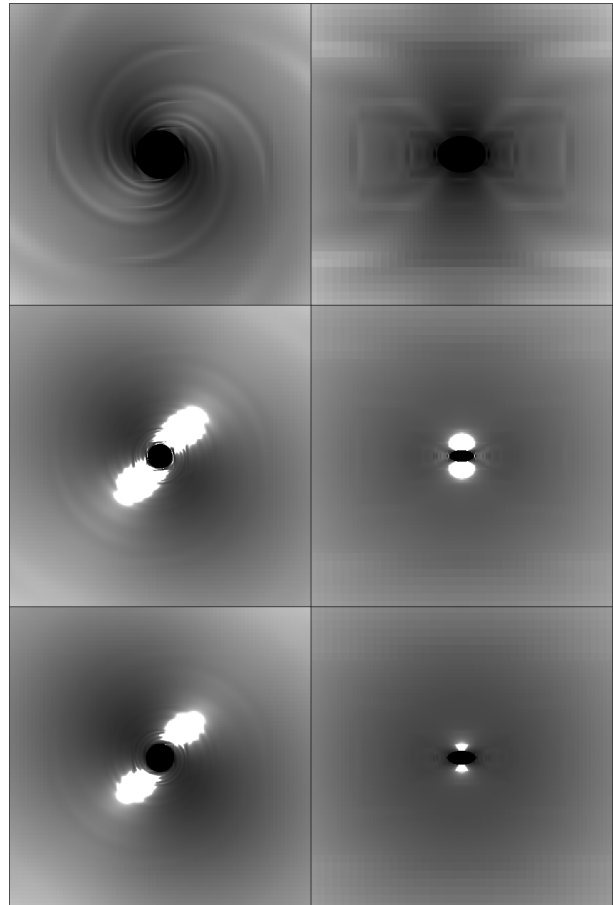


FIG. 5: Snapshots of  $\mathcal{N}$  computed from Eq. (40). From top to bottom, case V3, V4 and V5 are shown. They correspond to times  $65.28M$ ,  $62.72M$ , and  $50.24M$  for V3, V4 and V5 respectively, and cover a region  $6M$  across. Left panels show a cut through the equatorial or  $z = 0$  plane. The right panels show the  $y = 0$  plane along the rotation axis of the BH. Gray shaded areas are those in which the null energy condition is violated. White areas in the V4 and V5 cases are regions with positive values of  $\mathcal{N}$ . The grayscale is logarithmic in absolute value, with a global minimum of  $-2 \times 10^{-4}$  for V3,  $-0.004$  for V4 and  $-0.004$  for V5.

As mentioned in Sec. II, one of the assumptions that the extremality condition  $\zeta \leq 1$  hinges on is the validity of the null energy condition. The null-energy condition states that for all null vectors  $k^a$

$$\mathcal{N} = T_{ab}k^ak^b \geq 0. \quad (38)$$



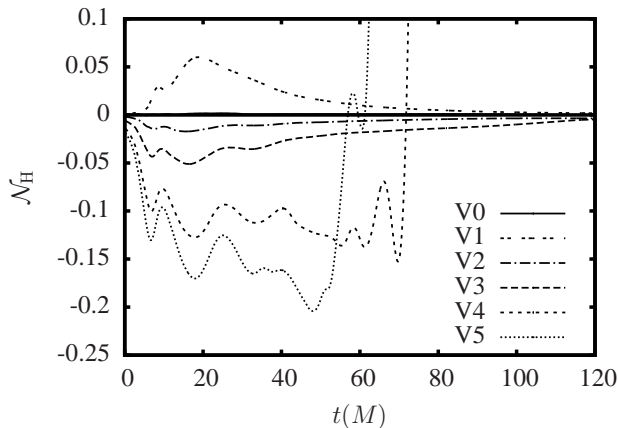


FIG. 6: Average of the null energy condition  $\mathcal{N}_H$  on the surface of the AH.

Substitution in Eq. (38) of the stress-energy tensor  $T_{ab}$  with the form given by Eq. (33) yields

$$\mathcal{N} = \frac{2}{3}\rho - 2j_a l^a + M_{ab}^{TF} l^a l^b. \quad (39)$$

Above, we have used a null vector  $k^a = n^a + l^a$  with  $l^a n_a = 0$  and  $l^a l_a = 1$ . If we choose  $l^a$  to be radial and centered at the BH, i.e.  $l^a = \hat{e}_r^a$ , then

$$\mathcal{N} = \frac{2}{3}\rho - 2j_r + M_{rr}^{TF}, \quad (40)$$

We have evaluated (40) throughout the computational domain. Not surprisingly, we found that for all the negative energy density cases the null energy condition is violated in regions near the BH. Figure 5 shows snapshots for the cases V3, V4 and V5. The left panels in Fig. 5 are snapshots of the equatorial or  $z = 0$  plane. The right panels are the  $y = 0$  plane along the BH rotation axis. White areas are regions with positive values of  $\mathcal{N}$ , and gray shaded areas those in which the null energy condition is violated. The grayscale is logarithmic in absolute value, with minima of  $-2 \times 10^{-4}$  for V3,  $-0.004$  for V4 and  $-0.004$  for V5.

The left panels in Fig. 5, showing the equatorial plane, make evident the formation of an inspiral (non-axisymmetric) structure in  $\mathcal{N}$  typically associated with BH accretion. Also interesting is that among the three cases depicted, only the one with the weakest negative energy shell, case V3, shows *no* region where the null energy condition is *not* violated. The right panels,  $y = 0$  or edge-on planes, show hints of a double diagonal structure. They are a consequence of cutting through the “thick accretion disk” that forms. For the case V3, grid effects are also noticeable because of the small values that  $\mathcal{N}$  takes.

We have also evaluated the null energy condition at the surface of the AH. That is, we evaluated  $\mathcal{N}_H = T_{ab} k^a k^b$  on the AH using the null vector  $k^a = n^a + s^a$ , with  $s^a$  the spatial unit normal to the AH. In Fig. 6, we show how the average of  $\mathcal{N}_H$  changes during the course of the

evolutions. The null energy condition is clearly violated in cases V2–V5. A closer look at the data shows that this null energy condition is violated not only on average, but also everywhere on the AH surface.

In summary, the violations of the null energy condition in the vicinity of the BH (Fig. 5) and on the surface of the AH (Fig. 6) demonstrates consistency with the violation of the extremality bound  $\zeta = 1$ .

## VII. CONSTRAINTS AND LATE BEHAVIOR

To understand the late behavior and, in particular, to get clues about the instability of the super-extremal BHs, we calculated the L2 norms of  $\rho$ ,  $j^i$  and  $\mathcal{G}^i$  within concentric shells  $1M < r < 2M$ ,  $2M < r < 4M$ , and  $4M < r < 8M$  as a function of evolution time. Figures 7, 8 and 9 show these L2 norms. First note that after  $t \sim 100M$  the L2 norms of  $\rho$ ,  $j^i$  and  $\mathcal{G}^i$  for the V0, V1 and V2 cases reach comparable levels. This signals that the V1 and V2 systems are settling down to a vacuum BH. Given that the BHs in V1 and V2 accreted matter, their final mass and spins will be different from those of V0.

Case V3 shows a different behavior. Initially,  $\rho$ ,  $j^i$  and  $\mathcal{G}^i$  drop and stabilize as with V1 and V2 as a consequence of matter having been accreted by the BH. The approximately constant values are, however, larger than the corresponding values in V1 and V2. Beyond,  $t \sim 250M$ ,  $\rho$ ,  $j^i$  and  $\mathcal{G}^i$  begin to grow as the BH approaches its maximum  $\zeta$  value at  $t \sim 300M$  (see Fig. 4).

Cases V4 and V5, those that led to super-extremal BHs, show more complex behavior. Initially, the slight drop of  $\rho$ ,  $j^i$  and  $\mathcal{G}^i$  in the outer two shells gives a hint of the undergoing accretion with the inner shell remaining approximately constant. Around the time the BH surpasses extremality,  $t \sim 65M$  for V4 and  $t \sim 45M$  for V5,  $\rho$ ,  $j^i$  and  $\mathcal{G}^i$  start growing appreciably. This smooth growth continues until  $t \sim 120M$  for V4 and  $t \sim 100M$  for V5. During this period,  $\zeta$  reaches a maximum value and proceeds to decrease. The decrease in  $\zeta$  is eventually accompanied with a decrease in  $\rho$ ,  $j^i$  and  $\mathcal{G}^i$ . At around  $t \sim 150M$  for V4 and  $t \sim 130M$  for V5, an ejection burst is triggered deep in the interior of the BH. Evidence of this ejected burst is the delay at which the burst emerges in each of the shells. That is, in Figures 7, 8 and 9 the burst shows in the solid line first, dash line next and dotted line last.

The L2 norms in Figures 7, 8 and 9 do not provide a good sense of the details of the dynamics of  $\rho$ ,  $j^i$  and  $\mathcal{G}^i$ . In Fig. 10 we display the temporal evolution of spatial features. We show snapshots of  $\rho$  for the V4 case in the equatorial plane (left) and axis plane (right) at times  $t \simeq 50M$ ,  $100M$ ,  $150M$ , and  $200M$  from top to bottom. The grayscale from top to bottom is such that [white:black] =  $[0 : -0.003]$ ,  $[0.08 : -0.08]$ ,  $[0.02 : -0.02]$ , and  $[0.008 : -0.008]$  respectively. The panels are  $5M$  across. The bottom left two panels clearly show a

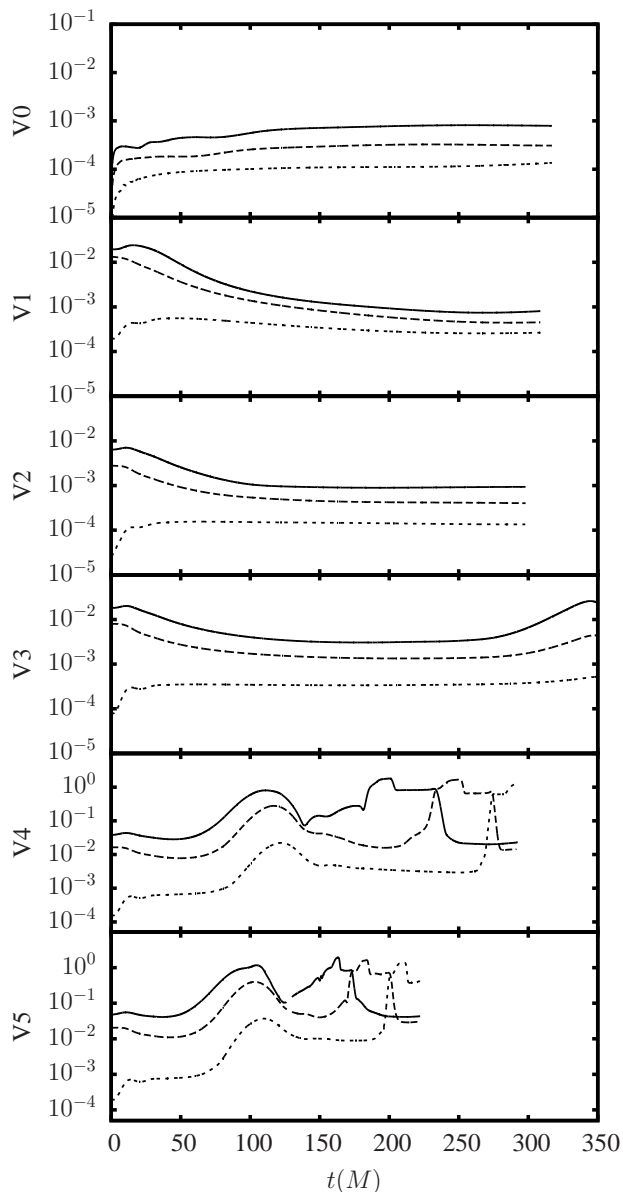


FIG. 7: L2 Norm of  $\rho$  (r.h.s. Hamiltonian constraint) in concentric shells:  $1M < r < 2M$  (solid),  $2M < r < 4M$  (dashed), and  $4M < r < 8M$  (dotted).

burst of negative energy. A similar burst is found in  $j^i$ , which explains the smaller value of  $\zeta$  during a brief period at  $t \sim 150M$  when the AH is again located. A detailed investigation of the late behavior of these super-extremal cases will be the subject of subsequent study.

### VIII. CONCLUSIONS

We have carried out a series of numerical experiments showing accreting BHs that violate the extremal spin condition  $\zeta \leq 1$ . The experiments consisted of a BH, modeled by a spinning puncture, surrounded by a

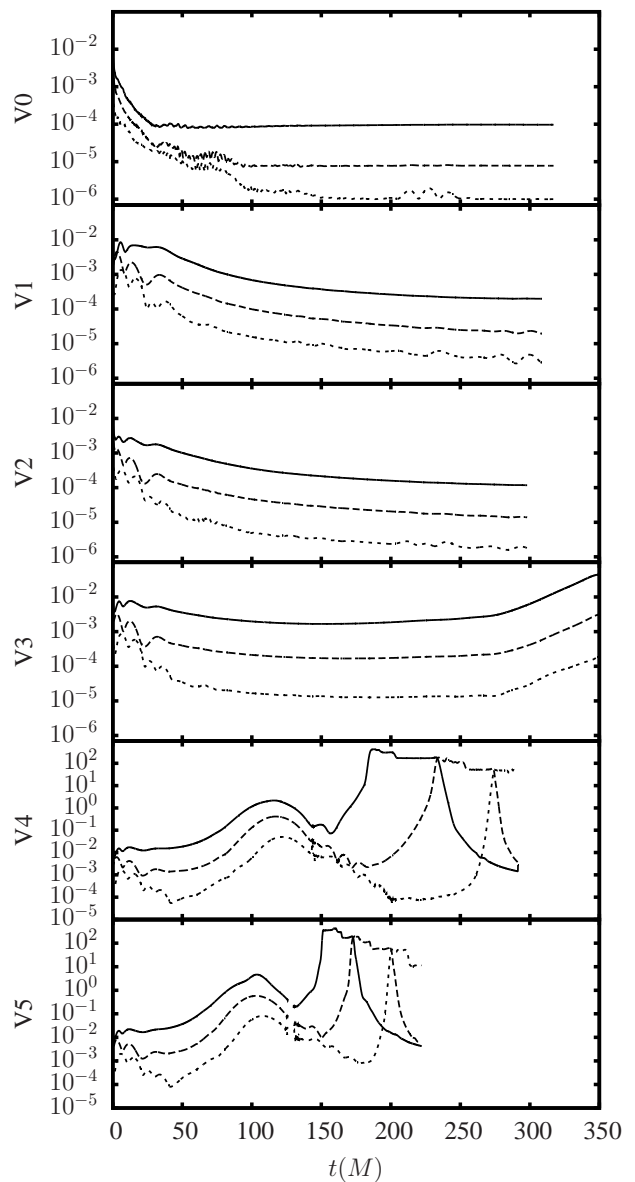


FIG. 8: L2 Norm of  $j^i$  (r.h.s. momentum constraint) in concentric shells:  $1M < r < 2M$  (solid),  $2M < r < 4M$  (dashed), and  $4M < r < 8M$  (dotted).

spherically-symmetric shell. We considered shells with positive energy density and negative angular momentum, but the main focus was shells with negative energy density and positive angular momentum. The idea behind this setup was that, as the BH accretes a negative energy, positive angular momentum shell, its mass will decrease and its spin will increase, leading to possible violations of the  $\zeta = 1$  extremality bound. We were successful in violating the extremality bound, at least temporarily. In agreement with the findings by Booth and Fairhurst [6], the violations were accompanied with violations of the null energy condition. The BHs that violated the  $\zeta = 1$  bound were not able to sustain super-extremality and simultaneously retain axisymmetry.

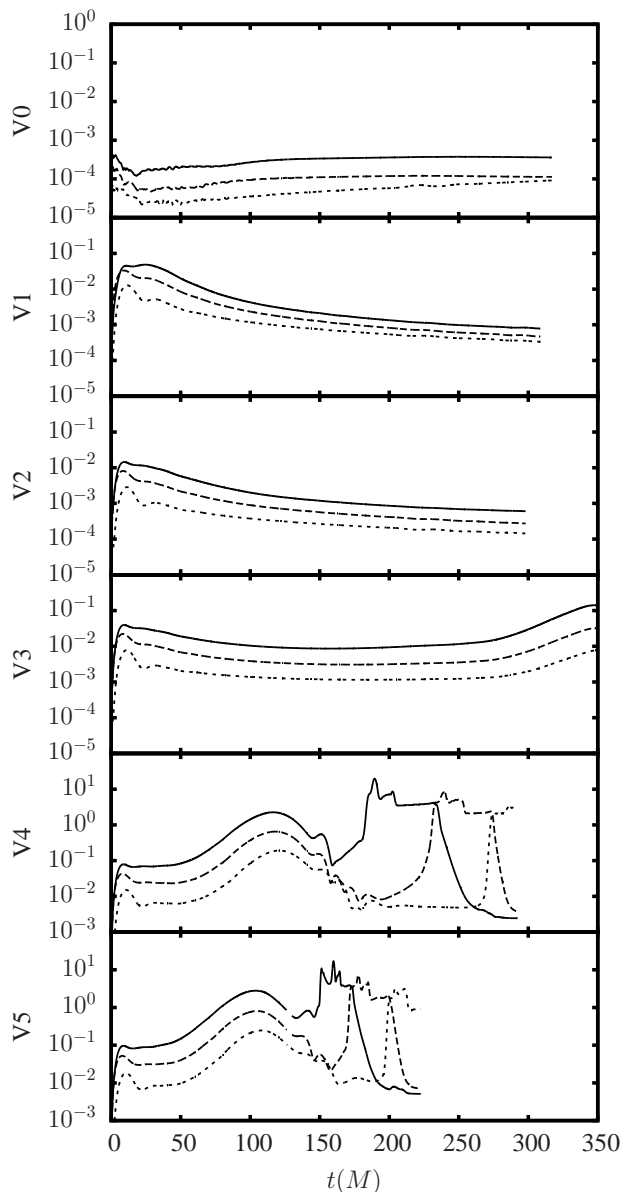


FIG. 9: L2 Norm of the connection constraint  $\mathcal{G}^a$  in concentric shells:  $1 M < r < 2 M$  (solid),  $2 M < r < 4 M$  (dashed), and  $4 M < r < 8 M$  (dotted).

Our results are also consistent with work by Jaramillo, Reiris and Dain [16] that appeared soon after the submission of our manuscript. The work in Ref. [16] proved that  $\zeta \leq 1$  holds for outermost stably marginally trapped surfaces that are axisymmetric in the presence of surrounding matter satisfying the dominant energy condition. The proof did not require axisymmetry of the exterior matter, only for the trapped surface.

The study involved several challenges. The most significant challenge was locating the AH as the BH became super-extremal. In subsequent work, we will investigate gauge conditions that could alleviate difficulties caused by the extreme deformations of the BH horizon. If a new

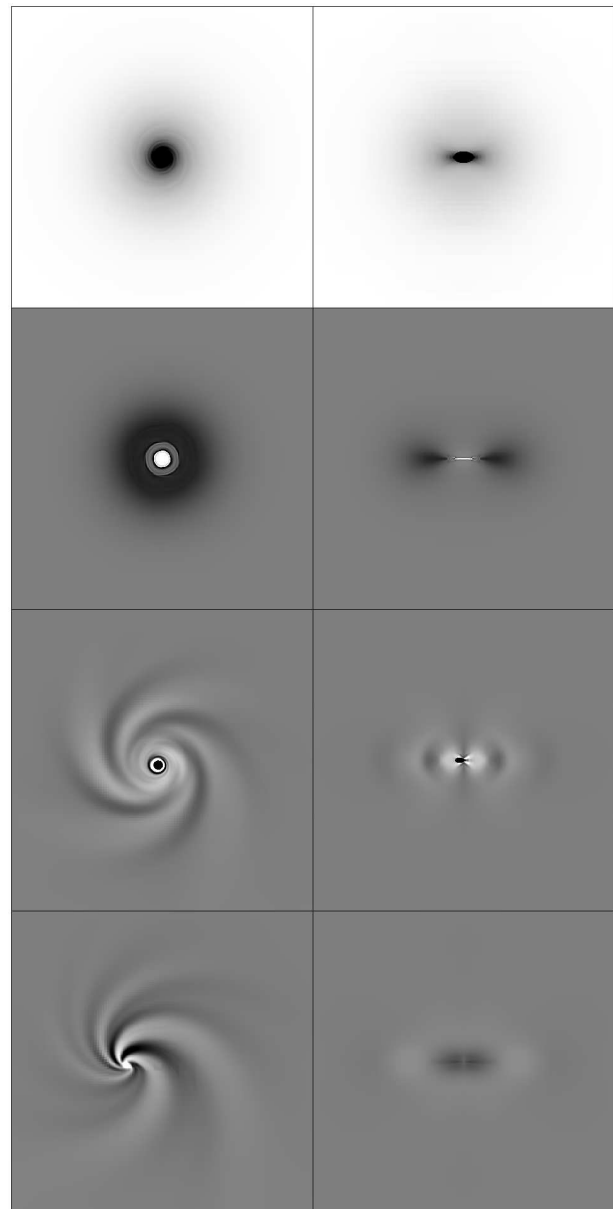


FIG. 10: Snapshots of  $\rho$  of the V4 case in the equatorial-plane (left) and axis-plane (right) at times  $t \simeq 50 M$ ,  $100 M$ ,  $150 M$ , and  $200 M$ . The grayscale from top to bottom is such that [white:black] =  $[0 : -0.003]$ ,  $[0.08 : -0.08]$ ,  $[0.02 : -0.02]$ , and  $[0.008 : -0.008]$  respectively. The regions, all centered about the coordinate origin, are  $5 M$  across.

gauge condition is found, we will be in a better position to investigate if violations of extremality are accompanied with the disappearance of the AH. We will also focus on the late-time behavior to get a better understanding of the causes behind the late emission responsible for the drop of the spin parameter  $\zeta$ .

Our study introduced a new approach to construct non-vacuum dynamical spacetimes: the *matter-without-matter* evolution framework. Under this approach, only the evolution equations are used, with the matter source

terms set to zero. Specifically, we demonstrated that the 3+1, BSSN vacuum evolution equations were capable of providing the dynamics of matter fields that are *invisible* to the equations. The price paid in MWM evolutions is restrictions on the “equations of state” satisfied by the matter content. It is not clear whether MWM evolutions could be applied to other 3+1 formulations of the Einstein equations and produce stable and convergent simulations.

### Acknowledgments

Work supported in part by NSF grants PHY-0914553, PHY-0855892, PHY-0903973, PHY-0941417. Computa-

tions carried out under TeraGrid allocation MCA08X009 and at the Texas Advanced Computation Center, University of Texas at Austin. We thank A. Ashtekar, S. Fairhurst, R. Haas, G. Lovelace and the anonymous referees for their comments and suggestions.

- 
- [1] M. Ansorg and H. Pfister, *Classical and Quantum Gravity* **25**, 035009 (2008), 0708.4196.
  - [2] J. Hennig, M. Ansorg, and C. Cederbaum, *Classical and Quantum Gravity* **25**, 162002 (2008), 0805.4320.
  - [3] J. Hennig, C. Cederbaum, and M. Ansorg, *Communications in Mathematical Physics* **293**, 449 (2010), 0812.2811.
  - [4] M. Ansorg and D. Petroff, *Phys. Rev. D* **72**, 024019 (2005), arXiv:gr-qc/0505060.
  - [5] G. Lovelace, R. Owen, H. P. Pfeiffer, and T. Chu, *Phys. Rev.* **D78**, 084017 (2008), 0805.4192.
  - [6] I. Booth and S. Fairhurst, *Phys. Rev.* **D77**, 084005 (2008), 0708.2209.
  - [7] A. Ashtekar and B. Krishnan, *Living Reviews in Relativity* **7**, 10 (2004), arXiv:gr-qc/0407042.
  - [8] K. S. Thorne, *Astrophys. J.* **191**, 507 (1974).
  - [9] T. W. Baumgarte and S. L. Shapiro, *Phys. Rev. D* **59**, 024007 (1999), arXiv:gr-qc/9810065.
  - [10] T. Bode et al., *Phys. Rev.* **D80**, 024008 (2009), 0902.1127.
  - [11] T. W. Baumgarte, S. A. Hughes, and S. L. Shapiro, *Phys. Rev. D* **60**, 087501 (1999), arXiv:gr-qc/9902024.
  - [12] C. F. Sopuerta, U. Sperhake, and P. Laguna, *Classical and Quantum Gravity* **23**, 579 (2006), arXiv:gr-qc/0605018.
  - [13] J. Healy, P. Laguna, R. A. Matzner, and D. M. Shoemaker, *ArXiv e-prints* (2009), 0905.3914.
  - [14] T. Bode, R. Haas, T. Bogdanovic, P. Laguna, and D. Shoemaker, *ArXiv e-prints* (2009), 0912.0087.
  - [15] D. Christodoulou, *Phys. Rev. Lett.* **25**, 1596 (1970).
  - [16] J. L. Jaramillo, M. Reiris, and S. Dain (2011), 1106.3743.
  - [17] T. W. Baumgarte and S. L. Shapiro, *Numerical Relativity: Solving Einstein's Equations on the Computer* (2010).
  - [18] S. Brandt and B. Brüggmann, *Physical Review Letters* **78**, 3606 (1997), arXiv:gr-qc/9703066.
  - [19] J. M. Bowen and J. W. York, Jr., *Phys. Rev. D* **21**, 2047 (1980).
  - [20] J. W. York, Jr., in *Sources of Gravitational Radiation*, edited by L. L. Smarr (1979), pp. 83–126.
  - [21] R. J. Gleiser, C. O. Nicasio, R. H. Price, and J. Pullin, *Phys. Rev.* **D57**, 3401 (1998), gr-qc/9710096.
  - [22] H. Bondi, *Rev. Mod. Phys.* **29**, 423 (1957).